ISBN: 978-3-95450-204-2 ISSN: 2673-5350 doi:10.18429/JACoW-IBIC2019-TUPP038

SPATIAL RESOLUTION OF AN X-RAY PINHOLE CAMERA USING A MULTI-LAYER MONOCHROMATOR

L. Bobb*, G. Rehm, Diamond Light Source, Oxfordshire, U.K.

Abstract

X-ray pinhole cameras are widely used for beam emittance monitoring at synchrotron light sources. Due to the reduction in beam emittance expected for the many fourth generation machine upgrades, the spatial resolution of the pinhole camera must be improved accordingly. It is well known that there are many contributions to the point spread function. However, a significant contribution arises from diffraction by the pinhole aperture. Given that diffraction is dependent on the spectral distribution of the incident synchrotron radiation, the spatial resolution can be improved by using a monochromatic beam. For optimal performance, the photon energy should be matched to the pinhole aperture size. Here we investigate the spatial resolution of the pinhole camera as a function of photon energy using a multi-layer monochromator.

INTRODUCTION

Emittance monitoring is a crucial diagnostic instrument at synchrotron light sources. With the planned upgrades to fourth generation synchrotrons such as Diamond-II [1], which are in part motivated by a reduction in emittance to provide increased brightness on beamlines, the emittance monitoring capabilities must be upgraded accordingly. Given the reduced emittance, the transverse size of the electron beam in the storage ring will also decrease. Thus the spatial resolution of the diagnostic instrumentation must be improved to ensure accurate measurement of the emittance for feedback systems [2].

The point spread function (PSF) defines the spatial resolution of the diagnostic instrument. For X-ray pinhole cameras (XPCs), as shown in Fig. 1, it is well documented that each optical element will contribute to the overall PSF. The PSF from each optical element is assumed to be Gaussian such that the overall PSF is

$$\sigma^2_{\mathrm{PSF}} = \sigma^2_{\mathrm{pinhole}} + \sigma^2_{\mathrm{camera}} \tag{1}$$

with

$$\sigma^2_{\mathrm{pinhole}} = \sigma^2_{\mathrm{diffraction}} + \sigma^2_{\mathrm{aperture}} \tag{2}$$

and

$$\sigma^2_{\mathrm{camera}} = \sigma^2_{\mathrm{screen}} + \sigma^2_{\mathrm{lens}} + \sigma^2_{\mathrm{sensor}} \tag{3}$$

where the subscripts denote the optical element of the PSF contributions [3, 4].

The fundamental PSF of a pinhole camera comes from the requirement of a pinhole aperture to form an image. As shown in Eq. (2) this aperture causes geometrical and diffraction effects to the propagating X-ray wavefront and is one of the largest contributors to the overall PSF. Although the PSF contribution from the pinhole $\sigma_{\mathrm{pinhole}}$ cannot be avoided entirely, it can be minimised by matching the pinhole aperture size and photon energy [4].

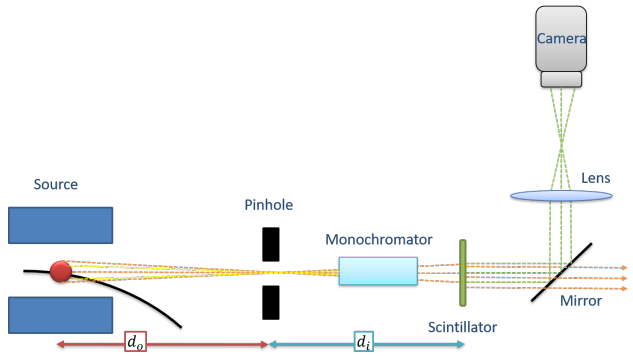

Figure 1: Schematic of an X-ray pinhole camera. The source-to-screen magnification is given by the ratio of the distances d_i/d_o.

PSF SIMULATION

Using XOP [5] a comparison of the spectral power distributions for the bending magnet source points in Diamond-I and Diamond-II is shown in Fig. 2. In all three cases similar spectral distributions are observed from 15 - 60 keV with the peak power in the 23 - 25 keV range. However due to the weaker magnetic field strengths of the Diamond-II dipoles (B_{D1} = 0.76 T, B_{D4} = 0.70 T), the total power is approx-

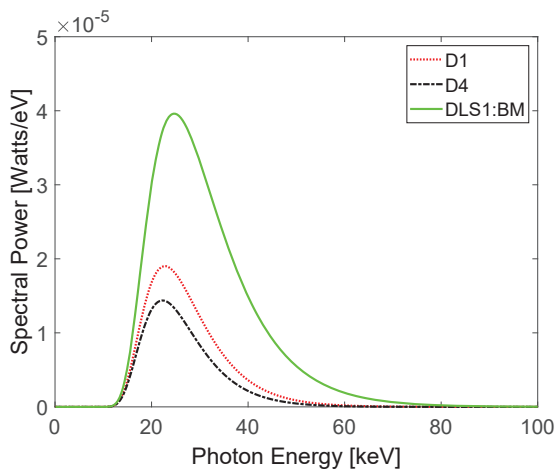

Figure 2: Comparison of the spectral power distributions, after 1 mm aluminium and 10 m air, of the bending magnet source points of Diamond-II (D1 and D4) with Diamond-I (DLS1:BM).

* lorraine.bobb@diamond.ac.uk

ISBN: 978-3-95450-204-2 ISSN: 2673-5350 doi:10.18429/JACoW-IBIC2019-TUPP038

imately one third of the power from a Diamond-I dipole ($B_{\mathrm{DLS1:BM}} = 1.4\,\mathrm{T}$). It should be noted that the beam energies are 3 GeV and 3.5 GeV for Diamond-I and Diamond-II respectively [1].

Using SRW [6] the vertical projection of the simulated PSF from a 25 µm×25 µm pinhole aperture for different photon energies in Diamond-I is shown in Fig. 3. The source-to-pinhole distance is 4.6 m. The pinhole-to-screen distance is 11.8 m. At low photon energies the PSF is well approximated by a Gaussian. As the photon energy increases the degree of quality to which the pinhole PSF can be approximated by a Gaussian is reduced. This can be understood by referring to the Fresnel number $N_F = A^2/(\lambda d_i)$ where A is the aperture size. For $N_F << 1$ Fraunhofer (far-field) diffraction occurs, otherwise Fresnel (near-field) diffraction occurs such that the pinhole PSF more closely resembles the pinhole aperture and the flattop is more pronounced [4].

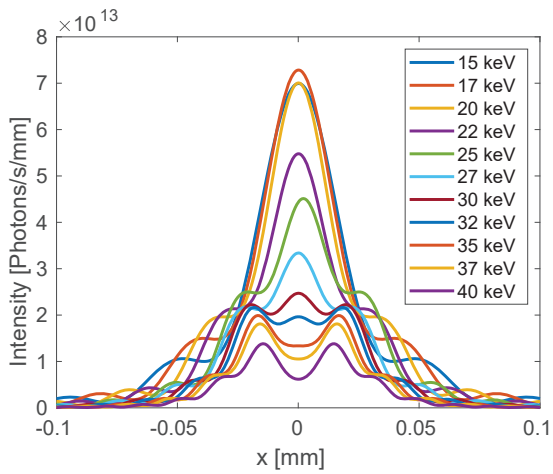

Figure 3: SRW simulation of the vertical PSF from a 25 µm pinhole aperture for different photon energies. This simulation does not include the attenuation of the X-rays from the 1 mm aluminium window and 10 m air.

EXPERIMENTAL SETUP

In the storage ring of Diamond there are three X-ray pinhole cameras: XPCs 1 and 2 are used for 24/7 operation of the vertical emittance feedback system, whereas XPC 3 is purpose built for research and development. Figure 1 shows the layout of the XPC where the distances d_o and d_i are 4.6 m and 11.8 m respectively. The source-to-screen magnification was measured to be 2.56. Approximately 4 m downstream of the sourcepoint, the X-rays transition from vacuum to air by passing through a 1 mm thick aluminium window. The X-ray beam then propagates through a 25 µm × 25 µm pinhole aperture formed by an assembly of tungsten blades and chemically etched shims [7]. The pinhole assembly is kept under a nitrogen environment to prevent oxidation.

On XPC 3, a single-bounce multilayer monochromator mirror was installed approximately 0.5 m upstream of the scintillator screen. The multilayer coating is Mo/Si with 100 layer−pairs deposited on float glass and has a d-spacing of 4.8 nm.

The full-width-half-maximum (FWHM) of a multilayer peak (in radians) is

$$\Delta\theta = \frac{\lambda}{m\Lambda} \tag{4}$$

where λ is the X-ray wavelength, m is the number of layer-pairs and Λ is the d-spacing (period) [8]. Using Eq. (4) at 20 keV the bandpass of the monochromator is 400 eV which gives $\Delta E/E \approx 2\%$.

The reflective surface of the monochromator is 300 mm × 50 mm. The horizontal size of the beam image σ_{xi} at the scintillator screen is approximately 150 µm. At 12 keV the estimated Bragg angle is approximately 12 mrad. If we assume the horizontal footprint of the beam is $6\sigma_{xi}$, the horizontal footprint of the beam at the scintillator screen is approximately 1 mm. For a monochromator orientated at 12 mrad with respect to the incident beam, the horizontal footprint of the beam image will span a length of 80 mm on the monochromator surface.

The monochromator is held under nitrogen inside a box with kapton windows to prevent oxidation. This system is then mounted on a rotation stage to select the photon energy, and a translation stage so it can be fully retracted from the beam path. Inside the box, the monochromator is mounted vertically such that the beam is reflected in the horizontal plane to preserve the vertical image distribution. Although the monochromator is installed close to the scintillator screen, due to the single-bounce setup the beam is deflected horizontally and must be tracked with the imager. In our case, the scintillator, mirror, lens and camera are mounted together on remotely controlled translation stages.

Initially the monochromator was aligned to a position parallel with the incident synchrotron radiation beam and the angle set point on the rotation stage was recorded as 0°. To calibrate the the beam angle and photon energy a Molybdenum filter with 0.1 mm thickness and an absorption edge at 20 keV was inserted in the beam path and the rotation angle at which the intensity reduced, i.e. at the absorption edge, was recorded at 0.37°. The difference in angle between these measured positions was consistent with the expectation from theory given the Bragg angle for 20 keV is 0.37°.

RESULTS AND DISCUSSION

Due to the orientation of the monochromator, only the vertical beam size is preserved at the image plane of the pinhole camera. Images were acquired at different photon energies. For the data analysis, image stacking was necessary due to the low intensity after the monochromator. A Gaussian fit was applied to each pixel column of the stacked image at each photon energy. The average beam size at the scintillator screen is plotted with the standard error as a function of photon energy in Fig. 4.

The PSF of the pinhole camera is calibrated using the Touschek lifetime [7]. With the monochromator retracted (i.e. white beam) the true vertical beam size at the scin-

ISBN: 978-3-95450-204-2 ISSN: 2673-5350 doi:10.18429/JACoW-IBIC2019-TUPP038

tillator screen was measured as 30.1 µm. From knife-edge measurements the PSF from the scintillator screen, lens and camera is 8 µm.

A Gaussian fit was applied to each simulated PSF from SRW (see Fig. 3). The sigma of the fitted simulated PSF was added in quadrature to the true vertical beam size at the scintillator screen and the contribution from the scintillator screen. The simulated beam size at the scintillator screen at each photon energy is shown in Fig. 4.

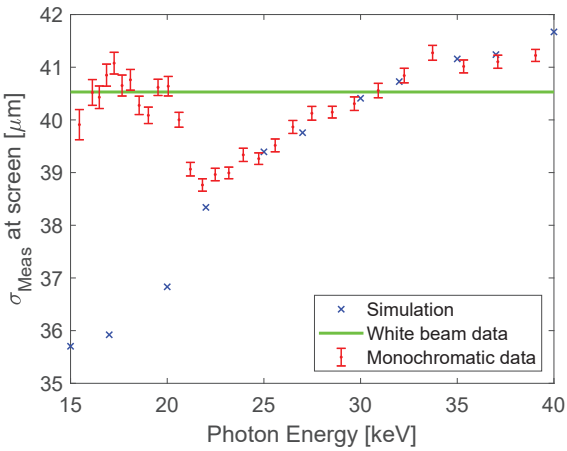

Figure 4: A comparison of the vertical beam size at the screen from measurement and simulation.

Figure 4 shows a good agreement of the measured and simulated vertical beam size at the scintillator screen for photon energies greater than 22 keV. The vertical beam size, from measurement and simulation, increases with photon energy. Below 22 keV the vertical beam size from simulation and theory diverge. Analysis proved more difficult over this range due to a low signal-to-noise ratio.

The measured beam size for white beam is also plotted alongside the monochromatic data. It is seen that a smaller beam size is simulated and measured for photon energies less than 30 keV in comparison to the white beam size measurement. Given that the true beam size of the electron beam in the storage ring was constant, with vertical emittance feedback enabled, the reduction in the measured beam size at different photon energies arises from a decrease of the PSF contribution. Thus it is demonstrated that the PSF contribution to the vertical beam size measurement is reduced by selecting a suitable monochromatic photon energy.

CONCLUSION

In this paper it has been demonstrated that the contribution from the aperture of the X-ray pinhole camera to the overall point spread function can be reduced by using monochromatic light. These first measurements with the recently installed multilayer monochromator have shown a good agreement with SRW simulations above 22 keV.

Further investigations are planned to improve the monochromatic X-ray pinhole camera. These studies will include testing a different multilayer monochromator and improving the capture efficiency of the photon yield using the microscope imager described in [9].

For Diamond-II the suitability of a monochromatic X-ray pinhole camera must be assessed. A lower flux is expected due to the weaker dipole field, thus a higher efficiency imaging system or direct X-ray detection will be needed especially for emittance feedback. Alternatively, the monochromator could be used for a complementary high resolution beam size monitor using X-ray interferometry. These options will also be investigated.

ACKNOWLEDGEMENTS

The authors would like to thank Kawal Sawhney, Stewart Scott and Graham Duller for the design of the monochromator. Thanks to Graham Cook and Martin Small for their contribution during the installation, and Michael Abbott for controls.

REFERENCES

[1] L.C. Chapon *et al.*, Diamond-II Conceptual Design Report, Diamond Light Source, Oxfordshire, UK, May 2019. https://www.diamond.ac.uk/Home/About/Vision/Diamond-II.html

[2] I. P. S. Martin, M. G. Abbott, M. Apollonio, D. Hickin, and R. Bartolini, "Operating the Diamond Storage Ring with Reduced Vertical Emittance", in *Proc. 4th Int. Particle Accelerator Conf. (IPAC'13)*, Shanghai, China, May 2013, paper MOPEA071, pp. 249–251.

[3] P. Elleaume *et al.*, "Measuring Beam Sizes and Ultra-Small Electron Emittances Using an X-ray Pinhole Camera", J. Synchrotron Rad., (1995). 2, pp. 209-214. doi:10.1107/s0909049595008685

[4] C. Thomas*et al.*, "X-ray pinhole camera resolution and emittance measurement", Phys. Rev. ST Accel. Beams 13, 022805, (2010). doi:10.1103/physrevstab.13.022805

[5] XOP, http://www.esrf.eu/Instrumentation/software/data-analysis/xop2.4

[6] O. Chubar and P. Elleaume, "Accurate and Efficient Computation of Synchrotron Radiation in the Near Field Region", in *Proc. 6th European Particle Accel. Conf. (EPAC'98)*, Stockholm, Sweden 22-26 June 1998, pp. 1177-1179.

[7] L. M. Bobb, A. F. D. Morgan, and G. Rehm, "Performance Evaluation of Molybdenum Blades in an X-ray Pinhole Camera", in *Proc. 5th Int. Beam Instrumentation Conf. (IBIC'16)*, Barcelona, Spain, Sep. 2016, pp. 795–798. doi:10.18429/JACoW-IBIC2016-WEPG63

[8] P. Willmott, *An introduction to synchrotron radiation: techniques and applications*, Second Ed., Wiley (2019), pp. 154.

[9] L. Bobb and G. Rehm, "Performance of a Reflective Microscope Objective in an X-ray Pinhole Camera", in *Proc. 7th Int. Beam Instrumentation Conf. (IBIC'18)*, Shanghai, China, Sep. 2018, pp. 477–481. doi:10.18429/JACoW-IBIC2018-WEPB18